Article

A Numerical Method for the Dynamics Analysis of Blade Fracture Faults in Wind Turbines Using Geometrically Exact Beam Theory and Its Validation

Xianyou Wu [1,*], **Kai Feng** [1] **and Qing'an Li** [2]

1 College of Mechanical and Vehicle Engineering, Hunan University, Changsha 410082, China; kfeng@hnu.edu.cn
2 Institute of Engineering Thermophysics, Chinese Academy of Sciences, Beijing 100190, China; liqingan@iet.cn
* Correspondence: wuxianyou@goldwind.com

Abstract: In pursuit of China's goals for carbon peak and carbon neutrality, wind turbines are continually evolving to achieve a lower levelized cost of energy. The primary technological focus in the wind power industry is on large-scale, lightweight designs for entire turbines to enhance cost competitiveness. However, this advancement has led to an increased risk of blade fractures under extreme operating conditions. This paper addresses this challenging issue by using geometrically exact beam theory to develop a nonlinear simulation model for long, flexible blades. The model accounts for sudden changes in blade properties at the moment of failure, covering both the extensive motions and deformations of the fractured blade. The validation of the proposed model is carried out by comparing the results from power production cases with bladed simulations and further validating the simulations of blade fracture load cases against measurement data. The methodologies and findings presented in this study offer valuable insights for diagnosing faults in wind turbines.

Keywords: wind turbine; nonlinear geometric large deformation; blade fracture; geometrically exact beam; aeroelasticity

1. Introduction

As China intensifies its commitment to the dual-carbon strategy, wind energy, a crucial renewable resource, faces market pressure to consistently reduce the cost per kilowatt-hour (kWh). The dominant trend in cost-effective wind turbine design combines high megawatt capacity with lightweight structures [1]. However, the shift towards larger megawatt designs using lightweight components significantly increases design risks, especially for long and flexible blades. Wind turbines operate under varied and complex natural conditions, including wind shear, yaw, and wind gusts, leading to frequent changes in wind direction and speed. As the primary load-bearing elements, blades endure nearly all of these forces and are highly prone to fractures. In recent years, incidents of turbine blade breakage have become more frequent, occasionally even causing tower failures. Simulating the load changes due to blade fractures can provide characteristic signals for blade faults, enabling early warnings. This capability is essential for ensuring wind turbine safety and developing effective preventative measures.

Several scholars have conducted research on wind turbine blade fractures. Carroll et al. [2] collected failure data from 350 offshore fixed-base wind turbines installed in Continental Europe, giving basic failure statistics for offshore wind turbines, including failure rate (8.3 failures/turbine/year) and mean time to failure (1055 h). Chen [3] analyzed blade fracture processes by considering factors such as field wind turbine speed, wind speed, power production, and fracture image analysis. Additionally, Eder et al. [4] introduced a virtual crack closure technique to identify critical areas associated with trailing edge cracking. Chen et al. [5] proposed a Bayesian deep learning model designed for predicting

the remaining service life of rolling element bearings in wind turbines, taking into account the first prediction time (FPT) and prediction uncertainty. This approach was validated using two published bearing datasets and demonstrated the effectiveness and validity of the model through experimental exploration. McGugan and Mishnaevsky [6] proposed a method for structural health monitoring of wind turbine blades that focuses on localized damage mechanisms. That approach includes the monitoring of various factors, such as leading-edge corrosion, adhesive failure, laminate buttresses, static and dynamic laminate testing, as well as bolt and laminate fatigue of wind turbine blades, enabling the monitoring and localization of specific damage mechanisms. Ji and Han [7] studied the failure behavior of adhesive joints in wind turbine blades, employing the fracture mechanics of the finite element analysis method, and presented an experimental verification of the method's correctness. Subsequently, they established a finite element model of the skin–web joint, utilizing the cohesive zone model to predict the initiation and propagation of damage. The results show stress concentration in the bonded joint, with shear stress identified as the primary factor leading to debonding. Focusing on the issue of delamination failure in wind turbine blade wing girder rim strips, Boyano et al. [8] used a mixed-mode test setup involving an end-notched flexure test with roller (ENFR) test method to measure and analyze the fracture behavior of carbon fiber-reinforced epoxy laminate specimens. The experimental data aligned with the theoretical values, thus illustrating the validity of the method in composite fracture testing. Furthermore, Rosemeier et al. [9] conducted numerical simulations, revealing the limitations of linear dynamic analysis for large blades, suggesting the use of nonlinear methods to improve failure simulation accuracy.

Studies have shown that wind turbine blades, being critical components for wind energy harvesting, experience prolonged exposure to cyclic wind loads, which makes them prone to fatigue damage, with the risk of fatigue failure being the main cause of wind turbine blade fracture. Wu et al. [10] used a rotating device for cyclic aerodynamic loading tests to investigate the strain response of bonded elongated composite wind turbine blades under nonconstant aerodynamic loading, and the results revealed a quadratic relationship between the strain value and the rotational speed. In addition, the study predicted fatigue damage in bonded elongated blades using nonconstant aerodynamic loading spectra, a rainflow cycle counting algorithm, Goodman plots, and Miner's principle of linear super-position. The results indicated that all materials used in the elongated blades, including UD fibers, 750 triaxial fibers, and structural adhesives, are safe enough for a 20-year design life. It was also observed that the bonded area is not the most vulnerable location regarding hazards. Chen et al. [11,12] conducted a comprehensive study in the structural collapse of large composite blades subjected to combined bending and torsion using a three-dimensional stress/strain domain progressive failure analysis method based on continuous damage mechanics. It simulates the failure behavior of large composite wind turbine blades, enabling accurate prediction of the progressive damage of composite materials. By measuring and analyzing the strain of the wind turbine blade, the study provided quantitative evidence of blade collapse, establishing that the root cause and damage mechanism of the structural collapse of large composite blades are attributed to the combined effects of bending and torsion. Epaarachchi and Clausen [13] used a finite element simulation method to establish a fatigue spectrum for small wind turbine blades by correlating periodic wind cyclic loads with blade stress cyclic loads, laying the foundation for subsequent fatigue analysis of blades. Boujleben and Ibrahimbegovic [14] proposed a simple and efficient computational model for addressing the strong fluid–solid coupling problem in wind turbine blades during steady-state flow. Coupled with an enhanced strain field, this model enables the calculation of the detailed blade stress distribution, which is of great significance for the prediction of blade fatigue failure risks. Zhang et al. [15] introduced a method for estimating the fatigue life of composite blades in horizontal-axis force turbines based on the modified blade element momentum theory and the finite element method. To validate the method, a 5 MW reference wind turbine blade from the National Renewable Energy Laboratory (NREL) was used as an example, showing that the proposed method serves as

an effective tool for evaluating the fatigue damage and structural performance of a wind turbine composite blade throughout its service life. Liu et al. [16] investigated the reliability of an offshore wind turbine blade with a floating foundation support through numerical calculations. They computed the probability of failure for blade root overload, blade root fatigue, and tip over displacement. They calculated and compared the failure probabilities of the blade with a fixed foundation support and the blade with a floating foundation support. The results indicated a significantly higher failure probability for the blade with a floating foundation support than for the blade with a fixed foundation support.

Existing studies mainly focus on analyzing blade fractures through field data, local strength simulations, fatigue damage mechanisms, and fatigue life analyses. However, there is a notable gap in examining the dynamic characteristics of wind turbines both before and after blade failures. These studies also lack the capability to reproduce wind turbine vibrations and the blade deformation process through simulation, limiting the support for blade break warnings and effective verification of emergency shutdown protection schemes.

Blade fractures leading to extreme conditions entail sudden changes in blade structural characteristics, large motion in translation and rotation, and large deformation beyond the normal design range, causing a typical strong nonlinear dynamics problem. The prevalent blade modeling method, commonly used in industry-specific simulation software, relies on the modal assumption method, which is based on a linear small deformation hypothesis without consideration of the impact of large deformation [17]. Despite the introduction of multipart modeling with modal assumptions to solve large deformation problems, the challenge of accurately updating the modal basis when structural characteristics change due to blade fracture remains [18]. The geometric stiffening effect, the axial foreshortening effect, and the complex bending–torsion–stretching effect could be captured with good accuracy by dividing the whole blade into more than 10 parts [19], but the computational efficiency is expected to decrease dramatically due to the large number of degrees of freedom. Therefore, the deformation process following blade fracture cannot be fully reflected using the existing modeling methods.

From a structural perspective, the blade fracture process entails sudden changes in structural characteristics at the fracture surface joint, extensive movement from the fracture surface to the blade tip, and significant deformation exceeding the design boundary. These sudden changes in the structural characteristics are generated due to abrupt status changes and external load impact. In the context of multibody dynamics analysis, three-dimensional large-scale motion, finite rotation, and large deformation in blade dynamics exhibit significant geometrical nonlinearity. These challenges can be tackled effectively using the absolute node coordinate formulation (ANCF) [20,21] and the geometrically exact beam (GEB) method [22]. Three different beam models are widely used, namely, Euler–Bernoulli beams, Timoshenko beams, and geometrically exact beams. The Euler–Bernoulli beam model [23], also known as the classical beam model, deals with slender beams subjected to tensile, torsional, and bending loads. The influence of the shear deformation is ignored in the model. The Timoshenko beam model [24] was firstly proposed by Timoshenko in the early 20th century. This model takes into account the shear deformation effect in the cross sections, making it more suitable for describing the behavior of thick beams than the Euler–Bernoulli beam model. For wind turbine blades that are typically slender, there is not much difference between the Timoshenko beam model and the Euler–Bernoulli beam model. Given the ease of implementation of the Euler–Bernoulli model, it has been adopted by many tools in the aeroelastic modeling of wind turbine blades. The geometrically exact beam model [25] is a newly developed beam model in recent years. Compared with the previous two beam models, it can capture the bending–torsion coupling of blades with a higher accuracy in case of large deformations [26]. The geometrically exact beam model employs the assumption of a flat section but does not make an approximation for the section rotation. As consequence, it can accurately handle the problems of large rotation and large deformation of beams [27]. In recent years, many scholars have applied it in the structural modeling of wind turbine blades [28,29] and the nonlinear dynamics analysis of

blades [30]. The introduction of geometrically exact beam models improves computational accuracy but also sacrifices computational efficiency. While the absolute node coordinate formulation sidesteps parameterization issues of finite rotation, it comes with the drawbacks of higher degrees of freedom and lower computational efficiency [31,32]. Conversely, the geometrically exact beam method offers high computational efficiency and accuracy, making it suitable for large-scale simulations in the wind turbine design stage [33,34].

Blade aerodynamic forces also experience significant changes during blade fractures. While the vortex wake-based method for calculating wind turbine blade aerodynamics has garnered attention [28,35], it still suffers from the disadvantage of high computational cost. Computational fluid dynamics simulation is the most accurate method but also the most expensive, and thus more often used in theoretical research on complex fluid dynamics or fluid–structure interactions (FSIs). Horcas et al. [36] studied the influence of a trailing edge flap on the vortex-induced vibration of a wind turbine blade using the FSI method. Grinderslev et al. [37] further investigated the sensitivities of the prescribed structural motion on the vortex-induced vibration. In the design phase of wind turbines and root cause analysis under various operational conditions, the computational efficiency of these advanced methods does not meet the timeliness requirements for design iterations. As a result, the theory of wind turbine aerodynamics remains predominantly based on the blade element momentum theory [38].

This paper introduces a structural nonlinear analysis model that incorporates blade fracture characteristics by integrating geometrically exact beam theory with blade element momentum theory. This model is designed to calculate changes in wind turbine vibration and blade deformation resulting from blade fractures. The results are compared with measurement data to validate the effectiveness of the proposed method.

2. Mathematical Model of Blade Fracture

2.1. Geometrically Exact Beam Theory

The blade sections experience large translations and rotations during the operation of wind turbines, as illustrated in Figure 1.
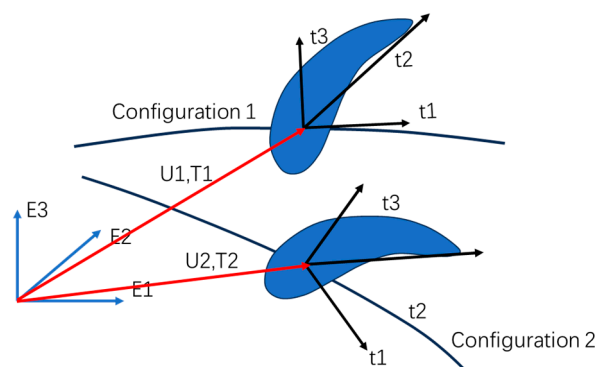

Figure 1. The deformation and movement of a blade section.

(E1, E2, E3) is the inertial frame of the system. (t1, t2, t3) is the local reference frame rigidly attached at the section. U is the position vector of the origin of the reference frame (t1, t2, t3) in the inertial frame (E1, E2, E3). T is the rotation tensor of the reference frame (t1, t2, t3) with respect to the inertial frame (E1, E2, E3). (U1, T1) and (U2, T2) describe two different configurations during the movement of the blade section.

The geometrically exact beam theory, which originated from the Reissner beam theory and evolved from the Timoshenko beam theory, relies on the assumption of a flat cross section [33]. In this study, quaternion parameterization is employed to precisely characterize the three-dimensional rotation of the flat cross section since the quaternion parameterization is free of singularity over the entire range of rotations [39].

$$\hat{q} = (q0, q) = (q0, q1, q2, q3) \tag{1}$$

where $q0$ is the scalar part of the quaternion, $\hat{q}$, and $[q1, q2, q3]$ is the vector part of $\hat{q}$.

The rotation tensor, Λ, along the reference line of the beam element is parameterized as follows:

$$\Lambda = \begin{bmatrix} q_0^2 + q_1^2 - q_2^2 - q_3^2 & 2(q_1 q_2 - q_3 q_0) & 2(q_1 q_3 + q_2 q_0) \\ 2(q_1 q_2 + q_3 q_0) & q_0^2 - q_1^2 + q_2^2 - q_3^2 & 2(-q_1 q_0 + q_2 q_3) \\ 2(q_1 q_3 - q_2 q_0) & 2(q_1 q_0 + q_2 q_3) & q_0^2 - q_1^2 - q_2^2 + q_3^2 \end{bmatrix} \tag{2}$$

The equations of motion, derived from the virtual work principle, as detailed in the literature [40], serve as the foundation for this investigation.

The virtual work of the internal forces can be integrated as below:

$$\delta W \int \left(\delta u'^{\mathrm{T}} \Lambda N + \delta \theta^{\mathrm{T}} \widetilde{u'}^{\mathrm{T}} \Lambda N + \delta \theta'^{\mathrm{T}} \Lambda M \right) dZ_{int} \tag{3}$$

where u is the transverse displacement and $\delta\theta$ is the virtual rotation vector representing the rotational deformation, which can be evaluated from the rotation tensor, Λ, as $\delta\theta = \text{axial}(\Lambda^{\mathrm{T}} \delta\Lambda)$, "axial" being the operator to extract the vector from a skew symmetric matrix; N, M are the sectional internal forces and moments, respectively; and $(\cdot)'$ refers to the derivative of the variable along the Z-axis of the reference frame (t1, t2, t3), $(\cdot)' = d(\cdot)/dZ$.

The virtual work performed by the external aerodynamic forces and gravitational forces can be evaluated as below:

$$\delta W_{ext} = \int \left(\delta u^{\mathrm{T}} f_a + \delta \theta^{\mathrm{T}} \Lambda \widetilde{\overline{R_a}} f_a + \delta \theta^{\mathrm{T}} m_a \right) dZ + \int \left(\delta u^{\mathrm{T}} A_\rho g + \delta \theta^{\mathrm{T}} A_\rho \Lambda \widetilde{\overline{R_g}} g \right) dZ. \tag{4}$$

where f_a, m_a are the aerodynamic forces and torques distributed along the beam element, respectively; $\overline{R_a}, \overline{R_g}$ are the position vectors of the aerodynamic center and the mass center with respect to the local reference frame, Λ, of the section, respectively; g is the gravity acceleration vector; and A_ρ is the mass per unit length of the cross section.

The virtual work performed by the inertial forces is expressed as below:

$$\delta W_{inert} = \int \delta u^{\mathrm{T}} A_\rho \ddot{u}_g dZ + \int \delta \theta^{\mathrm{T}} \left(A_\rho \Lambda \widetilde{\overline{R_g}} \ddot{u} + I_\rho \ddot{\theta} + \widetilde{\dot{\theta}} I_\rho \dot{\theta} \right) dZ. \tag{5}$$

where $\ddot{u}_g$ is the translational acceleration vector of the mass center; $\dot{\theta}$, $\ddot{\theta}$ are the angular speed and acceleration vectors of the mass center, respectively; I_ρ is the tensor of the mass moment of inertia of the cross section; and $\widetilde{(\cdot)}$ is the operator to obtain the skew symmetric matrix of a vector.

The summation of the virtual work of internal forces, external forces, and inertial forces is zero, leading to the balance equation of motion:

$$\delta W_{int} - \delta W_{ext} + \delta W_{inert} = 0 \tag{6}$$

The detailed process to substitute Equations (3) to (6) into the element discretized balance equations is outlined in the literature [33].

In this paper, the Newton–Raphson method is employed for iteratively solving the nonlinear balance equations. This method utilizes a tangent matrix to expedite the solution process during iterations. Given the complexity of the motion equations for geometrically exact beams, numerical differentiation methods are typically employed. However, in the context of blade fracture dynamics, when the structural contribution in the system tangent matrices changes significantly, numerical differentiation methods may encounter

the numerical instability issue due to abrupt changes in gradients. Consequently, this paper adopts an analytical linear increment equation to solve the problem.

2.2. Blade Element Momentum Theory

Blade element momentum theory is a classical method for aerodynamic calculations in wind turbine simulation [38,41]. By combining the blade element theory and momentum theory considering axial and azimuthal induction losses, it can provide a reasonably accurate distribution of aerodynamic forces in quasi-static states. However, as this method is based on static assumptions, practical applications often require corrections using engineering methods to account for dynamic characteristics. In general, the engineering methods include the correction models of dynamic stall, dynamic inflow, tip loss, turbulent wake state, skewed wake, etc.

As in the structural dynamics model, in the context of aerodynamics, the blade is discretized into a series of elements along the spanwise direction. The aerodynamic forces of each aerodynamic element are evaluated according to the thin airfoil theory. The inflow velocity surrounding a rotating blade station is schematized in Figure 2.
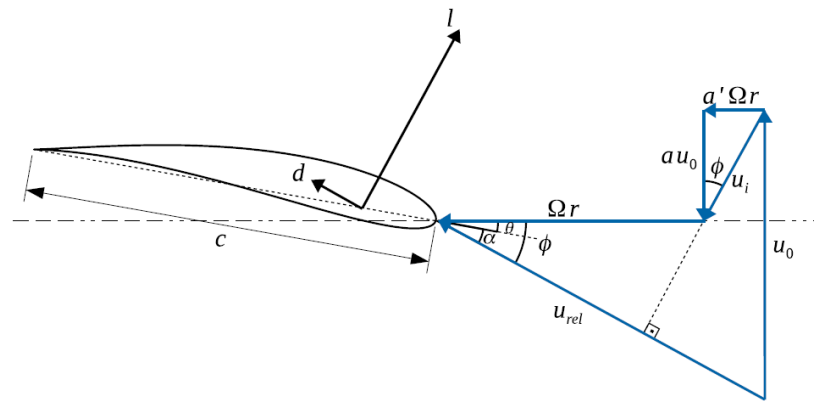

Figure 2. The velocity triangle of a rotating blade station.

The chord length of the blade station is c. r is the radius position with respect to the rotating center. Ω is the rotor rotational speed. u_0 is the velocity of the upcoming free inflow. a, a' are the axial and tangential induction factors, respectively. Correspondingly, au_0, $a'\Omega r$ are the axial and tangential induced velocities, respectively, representing the change in the inflow velocity due to the rotation of the airfoil. The combined induced velocity is $u_i = \sqrt{(au_0)^2 + (a'\Omega r)^2}$, and ϕ is the inflow angle. θ is the angle between the chord line and the rotating plane, which is the summation of the pitch angle, the pre-twist angle of the blade station, and the torsional deformation angle. The angle of attack is $\alpha = \phi - \theta$. l, d are the aerodynamic lifting and drag forces, respectively.

As depicted in Figure 2, the calculation of the relative inflow velocity for each blade element is expressed as follows:

$$u_{rel} = u_0 + u_i - \Omega \times r \tag{7}$$

The angle of incident flow is given by:

$$\phi_{ref} = \tan^{-1}\left(\frac{u_{y\_ref}}{-u_{x\_ref}}\right) \tag{8}$$

where u_{x_ref}, u_{y_ref} are the components of the relative inflow velocity in the rotating plane and out of the plane, respectively.

The calculation of thrust, dT, and torque, dM, for each blade element is:

$$dT = B\frac{1}{2}\rho u_{rel}^2 c(C_l \cos\varphi - C_d \sin\varphi)dr. \tag{9}$$

$$dM = rB\frac{1}{2}\rho u_{rel}^2 c(C_l \sin\varphi - C_d \cos\varphi)dr. \tag{10}$$

where C_l, C_d are the lifting and drag coefficients obtained through a linear interpolation in the polars with the solved angle of attack, α; ρ is the air density; and B is the number of blades in the rotor (typically, $B = 3$).

Concurrently, leveraging the momentum theorem yields:

$$dT = 4\pi r\rho u_0^2 a(1-a)dr. \tag{11}$$

$$dM = 4\pi r^3 \rho\Omega u_0 a'(1-a)dr. \tag{12}$$

The aerodynamic forces for each section can be derived by solving Equations (7)–(12) simultaneously. The model presented in this paper incorporates corrections for tip loss, dynamic inflow, and skewed wake. The calculation for the tip loss correction coefficient is expressed as follows:

$$F_r = \frac{2}{\pi}\arccos\left[\exp\left(-\frac{B}{2}\frac{R-r}{r\sin\varphi}\right)\right]. \tag{13}$$

where R is the rotor radius.

The corrected thrust and torque are determined by:

$$dT = 4\pi r\rho u_0^2 a(1-a)Fdr. \tag{14}$$

$$dM = 4\pi r^3 \rho u_0 \Omega a'(1-a)Fdr. \tag{15}$$

The dynamic inflow correction is given by two first-order filters, as below:

$$\begin{cases} \tau_1\frac{d\bar{u}_n}{dt} + \bar{u}_n = \bar{v}_{qsn} + k_w\tau_1\frac{d\bar{v}_{qsn}}{dt}, \\ \tau_2\frac{d\bar{v}_n}{dt} + \bar{v}_n = \bar{u}_n. \end{cases} \tag{16}$$

where $\bar{v}_{qsn}$ is the average induced velocity in the normal direction, $\bar{u}_n$ is an intermediate variable in the filters, and $\bar{v}_n$ is the final filtered value of the relative inflow velocity. The time constant coefficients are specified as $\tau_1 = \frac{1.1}{1-1.3a}\frac{R}{V_0}$, $\tau_2 = \left[0.39 - 0.26\left(\frac{r}{R}\right)^{\wedge}2\right]\tau_1$, $k_w \approx 0.6$. V_0 refers to a reference inflow speed in the rotor plane.

The correction for dynamic skewed wake is expressed as follows:

$$u_{i,x}(\Psi) = u_{i,x}\left(1 + k_x\left(\frac{r}{R}\right)\sin(\Psi) + k_y\left(\frac{r}{R}\right)\cos(\Psi)\right), \tag{17}$$

where $k_x = \tan\left(\frac{\chi}{2}\right)$, $k_y = 0$, Ψ is the relative azimuth angle, and χ is the skewed angle of the relative inflow velocity.

2.3. Coupled Simulation of the Blade Fracture Process

A modern wind turbine consists of three blades and a tower, connected by the hub and nacelle assemblies, in which the power transmission subsystem is placed. The three blades and the tower are modelled with the proposed geometrically exact beam formulation. The mechanical part in the power transmission subsystem is discretized as a series of rigid bodies. Holonomic constraints are applied to set up the connections between the rigid bodies and the beams. The foundation at the tower bottom is connected to the ground via a bushing element to reflect the flexibility of the soil–structure interaction. The external controller, provided as a dynamic link library file, specifies the demand values of the pitch

angles and the generator torque to stabilize the rotor rotational speed and maximize the power output.

The time-domain simulation process for the aerodynamic–structural coupling during the blade fracture process is elucidated in Figure 3. The simulation employs a fluid–structure weak coupling method with a fixed-step iteration approach. In each iteration, considering the current overall system state, the aerodynamic loads on the blades are computed using the blade element momentum theory. The Hilber–Hughes–Taylor alpha (HHT-alpha) method is employed to update the subsequent overall system state, refresh the global motion equations, and compute the equation residual. Once the convergence condition is satisfied, the calculation for the current step is completed, and the simulation proceeds to the next step. Otherwise, the process iterates using the Newton–Raphson method again.
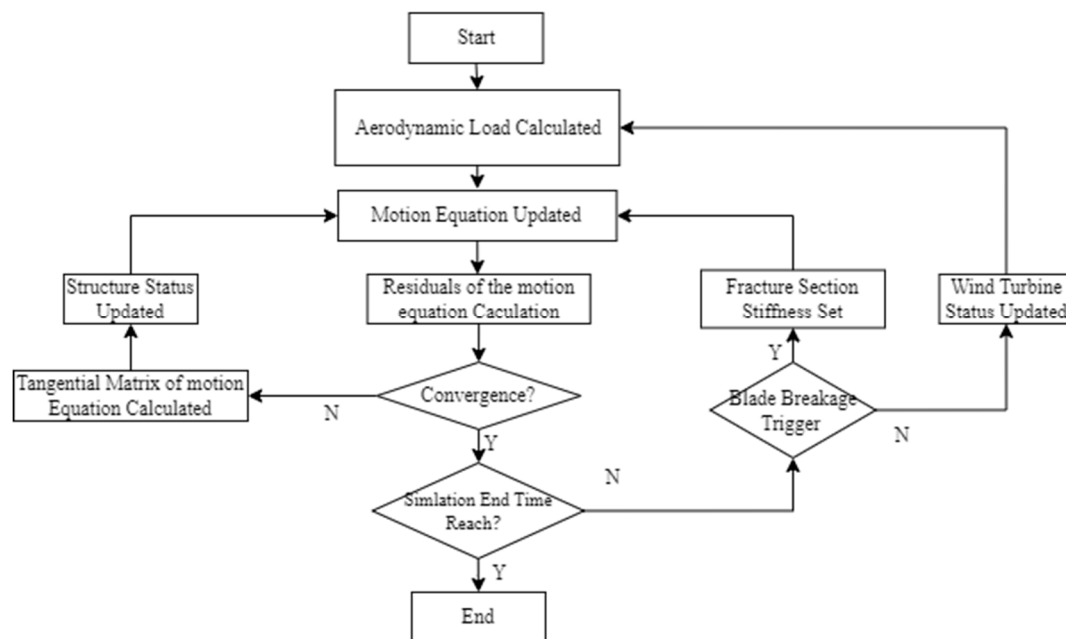

Figure 3. The simulation scheme of fracture blade dynamics.

During the iterative process, when the current time reaches the moment of blade fracture, the blade fracture algorithm is activated. This algorithm involves updating the blade cross-sectional stiffness settings, refreshing the overall system state equations, and updating the tangent matrix for that time step. If the equation residuals continuously increase for three consecutive steps, it is determined that the solution does not converge. In such instances, the step size is automatically reduced, and the variable step size method is employed to solve the state at that moment. After achieving convergence, the solver reverts to the fixed-step method.

To mitigate the impact at the beginning of the time integration, a quasi-static equilibrium analysis is carried out as the initialization. In the initialization phase, a normal wind profile with a constant wind speed is specified together with proper pitch angles. The inertial forces including the centrifugal forces and gyroscopic torques are tackled as external forces. Taking into account the internal elastic forces, the external inertial forces, the external constant aerodynamic forces, and the gravitational forces, the Newton–Raphson iterations are used to search for the quasi-static equilibrium configuration of the system. Once the equilibrium status is determined, the system-wise position, velocity, acceleration vectors, and constraints are stored as the initial conditions in the following time-domain dynamics simulation.

The typical location of blade fracture is generally at one-third of the distance from the root to the tip. Two fracture modes are considered: complete fracture and partial fracture.

Complete fracture occurs when the fracture completely separates from the blade tip after the blade fractures. In contrast, partial fracture involves a reduction in stiffness at the fracture location, leading to only partial mass loss. For simulations involving complete fracture, this paper adopts a method of releasing element constraints to update the global motion equations. Simulations involving partial fracture utilize the previously mentioned method of updating beam cross-sectional stiffness at the moment of blade fracture. A schematic diagram of blade fracture location and deformation is presented in Figure 4.

sudden changes in blade properties (broken section axis stiffness, bending stiffness and torsion stiffness) at the moment of failure
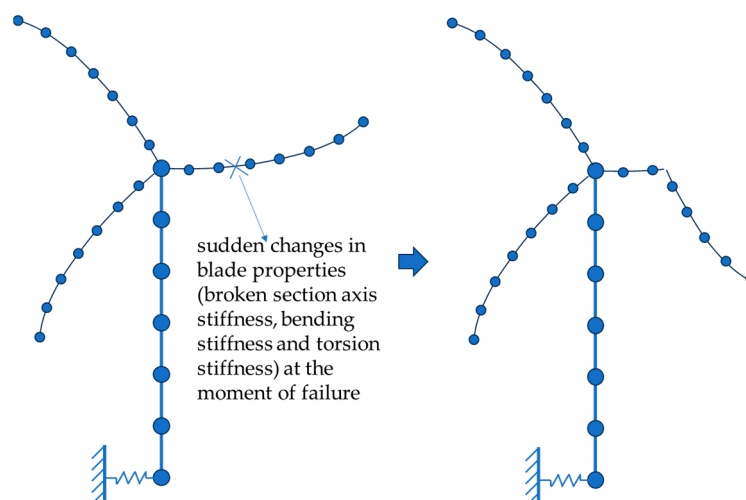
Figure 4. Diagram of blade fracture location and deformation.

The schematic diagram, Figure 4, reveals significant deformation after the blade fractures. Blades with partial fractures are prone to impact the tower due to the sudden decrease in local stiffness. However, as the collision process involves material nonlinear changes, the current paper does not consider reproducing the blade–tower collision and subsequent wrapping process.

3. Calculations, Results, and Analysis

To verify the accuracy of the algorithm, this study employed a realistic wind turbine model with a rotor diameter of approximately 155 m and a power capacity of 4.5 MW for a simulation analysis to compare the algorithm with Bladed [42], which is a commercial tool widely used in wind energy industry for over 20 years. Due to the requirement for confidentiality, the model data and the following measurement data obtained from a top commercial wind turbine manufacturer are not disclosed in this study.

3.1. Simulation Algorithm Verification

Before employing the proposed aeroelastic model to analyze the dynamics in the blade fracture process, a code-to-code verification was performed to examine the correctness of the mathematical model.

The operational status under normal operating conditions was compared against Bladed. The simulated wind speeds ranged from 5.5 m/s to 23.5 m/s with six turbulent seeds for each wind speed. In Bladed, a multipart blade model with five segments was used to account for the geometric nonlinearity in the large deformation of blades.

Initially, the static comparison results for the operational status at various wind speeds are presented in Table 1. The mean values of the pitch angles, rotor speed, and electrical power were analyzed for the various wind speeds. At the lowest wind speed, 5.5 m/s, the relative differences in the rotor speed and electrical power reach the highest value, 1.21%, attributed to differences in the Glauert empirical correction algorithm. The difference of 1.21% in the electrical power output may affect the business compactivity, but thanks to the low equivalent hours at a wind speed of 5.5 m/s, the overall influence is acceptable. The absolute differences in the pitch angles are less than 0.2 degrees at all wind speeds, which

is an excellent agreement. The relative differences in the pitch angles at wind speeds of 9.5 m/s and 11.5 m/s are higher than those at other wind speeds, mainly because of the small absolute values of the pitch angles around the rated wind speeds.

Table 1. Comparison of mean values of wind turbine status at various wind speeds.

Wind Speed/(m/s)	Pitch Angle/°		Rotor Speed/RPM		Electrical Power/kW	
	Diff.	Rel. Diff.	Diff.	Rel. Diff.	Diff.	Rel. Diff.
5.5	0.00	0.00%	0.08	1.21%	31.70	1.21%
7.5	−0.01	2.37%	0.07	0.78%	36.40	0.78%
9.5	−0.07	−10.87%	0.01	0.13%	−3.47	0.13%
11.5	−0.18	−4.46%	0.00	−0.01%	−8.26	−0.01%
13.5	−0.17	−2.23%	0.00	0.00%	−0.69	0.00%
15.5	−0.12	−1.15%	0.00	0.00%	−0.19	0.00%
17.5	−0.08	−0.64%	0.00	−0.01%	−0.21	−0.01%
19.5	−0.04	−0.25%	0.00	−0.01%	0.24	−0.01%
21.5	−0.04	−0.17%	0.02	0.19%	9.39	0.19%
23.5	0.06	0.18%	0.00	0.00%	0.58	0.00%

In the second step, the blade root loads were compared between the proposed method and Bladed. The comparative results for the three most important components, the flapwise moment, the edgewise moment, and the torque at the blade root, are presented in Figures 5–7, respectively. The relative deviations of this study from Bladed are also provided. The results in these figures have been normalized with respect to the overall operational mean values.
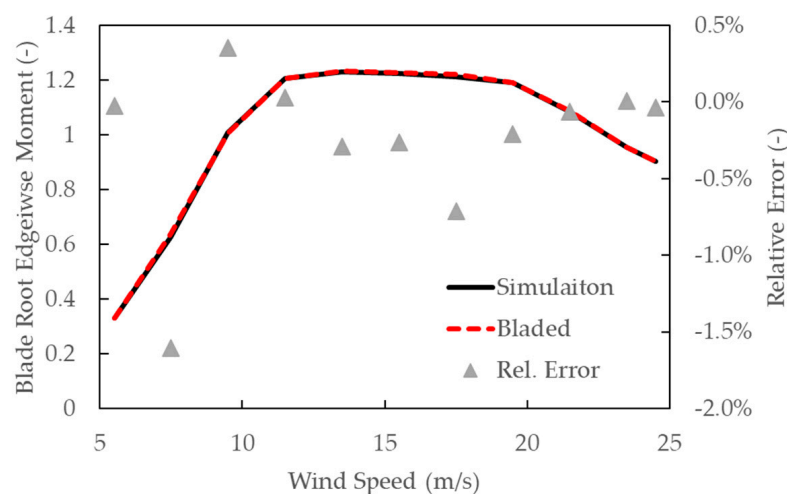

Figure 5. Comparison of mean values of blade root edgewise moment of each wind speed bin.

The blade root edgewise moment is mainly constitutive of the gravitational forces and the aerodynamic lifting forces projected in the rotor rotating plane. The contribution of the gravitational forces is eliminated in the mean values since the sign flips exactly at the rotor azimuth positions of 90 degrees and 270 degrees. The effective in-plane aerodynamic forces are the main source of the mean values of the blade root edgewise moment, as shown in Figure 5. The relative errors are within 1.5%, which is consistent with the difference level of the rotor speed and electrical power in Table 1.

The blade root flapwise moment primarily comprises the aerodynamic lifting forces out of the rotor rotating plane, which are the main source of wind turbine fatigue loads. The mean values of the blade root flapwise moment climb up to the highest point from 5.5 m/s to 9.5 m/s because of the increase in the wind speed and rotor speed. As can be seen, they turn to descend continuously in an approximately linear function after the wind

speed of 10 m/s is reached due to the pitch action. The relative errors are within 2.0% in all wind speed bins.
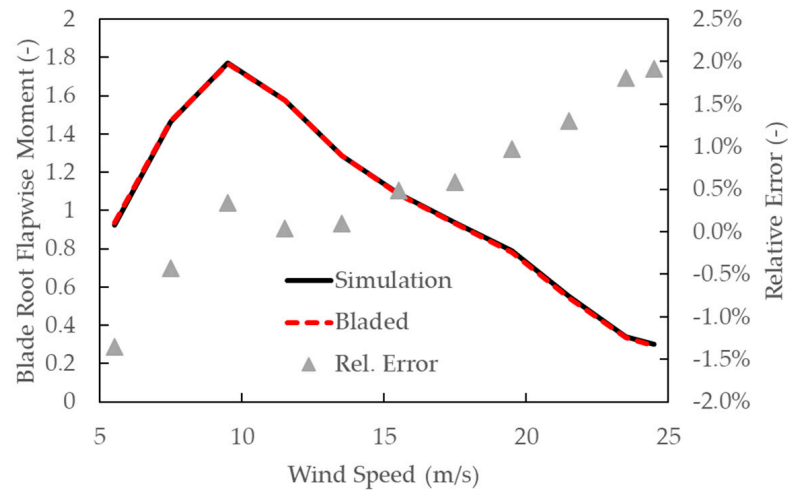

Figure 6. Comparison of mean values of blade root flapwise moment of each wind speed bin.
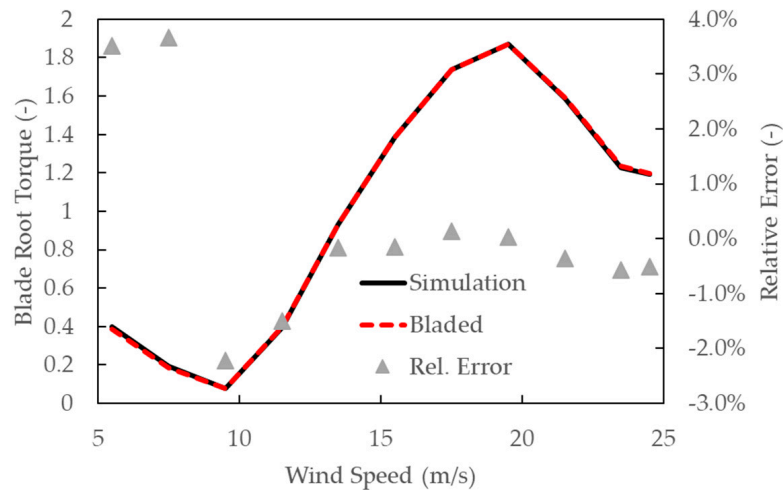

Figure 7. Comparison of mean values of blade root torque of each wind speed bin.

The blade root torque comes from the aerodynamic torque along the blade plus the contribution of the moments generated by the aerodynamic lifting forces in case of large blade deformation. The computation of the second part involves the accurate modelling for the complex bending–twist coupling in the large blade deformation. The amplitude of the blade root torque is generally much smaller than that of the blade root flapwise and edgewise moments, making it more difficult to obtain a good agreement. However, in this study, relative errors within 4.0% were observed for the blade root torque in all wind speed bins, implying that the complex bending–twist coupling of the blade is accurately captured.

As the last step of the code-to-code verification, the time series of the blade root M_{xy} at the rated wind speed of the design load case of normal power production was examined, as shown in Figure 8. The average amplitude of the blade root M_{xy} reaches a maximum at the rated wind speed, and thus the time series in Figure 8 is a representative one. It can be observed that the fluctuation period and amplitude of M_{xy} calculated in this study closely match those of Bladed, with minimal frequency component discrepancies.

Through the code-to-code comparisons, it is evident that the simulation results of the proposed method and Bladed are consistent. Both the statistical results for operational status and the transient time series of loads are in good agreement. Thanks to the multipart modal superposition algorithm, Bladed can also effectively simulate the nonlinear

deformation characteristics of blades. This verification underscores the accuracy of the proposed simulation model in calculating the nonlinear deformation of blades under normal operating conditions.
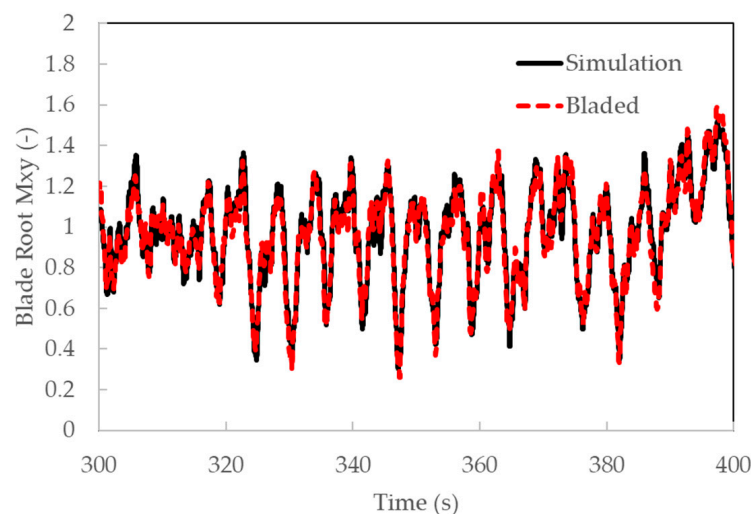

Figure 8. Comparison of time series of blade root M_{xy} at rated wind speed.

3.2. Validation with Field Measurements

A code-to-measurement comparison was conducted to validate the proposed simulation model. A prototype wind turbine with a 155 m rotor diameter was provided by the aforementioned commercial wind turbine manufacturer. A met mast, equipped with calibrated anemometers and wind vanes, was installed at the site to measure the wind resource for the prototype turbine. The strain gauges at the blade root and the tower bottom were equipped to measure the mechanical loads. The strain gauges were calibrated to comply with the international standard IEC 61400-13 [43]. The time series of the measured mechanical loads, together with the wind speed, wind direction, rotor speed, pitch angles, electrical power, etc., were recorded in the measurement system with a sampling frequency of 50 Hz. The measurement data were categorized according to the wind speed bins. The number of effective sample data for each wind speed bin satisfied the requirements of the international standard IEC 61400-13. The measurement campaign, lasting for more than three months, was carried out by test engineers of the wind turbine manufacturer.

The average values of air density, wind misalignment, wind shear, wind inflow angle, and turbulence intensity of each wind speed bin were extracted from the measurement data and then specified in the simulations accordingly. The dynamics simulations swept the wind speed range from 3 m/s to 20 m/s with an interval of 1 m/s. The mean values, the maximum and minimum values of the blade root flapwise moment, the edgewise moment, and the tower bottom fore–aft moment were analyzed in the post-processing of the simulations. The comparisons against the test data are shown in Figures 9–11. The sample number at the wind speed of 19 m/s was below the lowest requirement because the average wind speed of that wind farm was lower in summer, such that the high wind speed occurred rarely. As a consequence, a comparison at the wind speed of 19 m/s is absent from this study.

As discussed in Section 3.1, the blade root edgewise moment is mainly composed of the gravitational forces and the in-plane aerodynamic forces. The uncertainty of the blade mass is generally small, leading to a precise computation of the gravitational forces. The in-plane aerodynamic forces are tuned by the controller to match the electrical power at the specified wind speed and hence tend to be consistent between the simulation and test. The overall agreement of the blade root edgewise moment between the simulation and the test was excellent, as depicted in Figure 9.
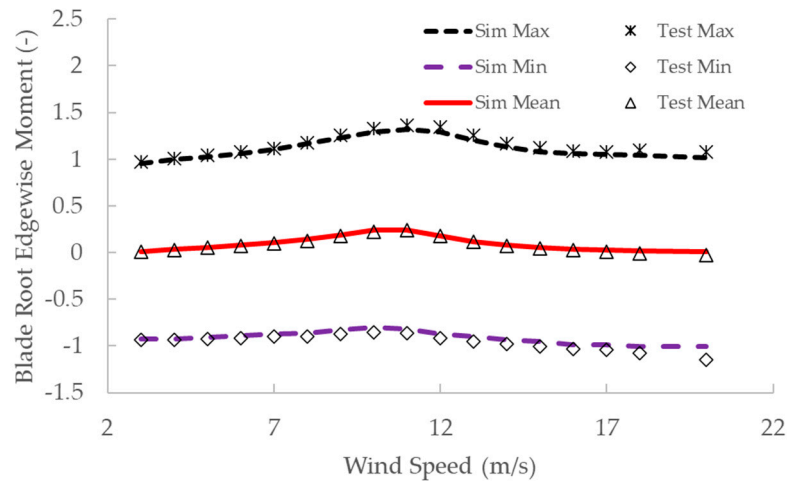
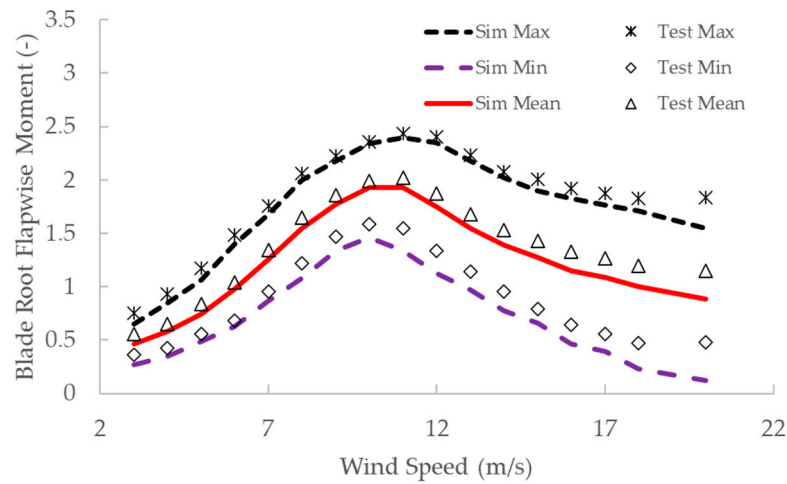**Figure 9.** Comparison of blade root edgewise moments of each wind speed bin.

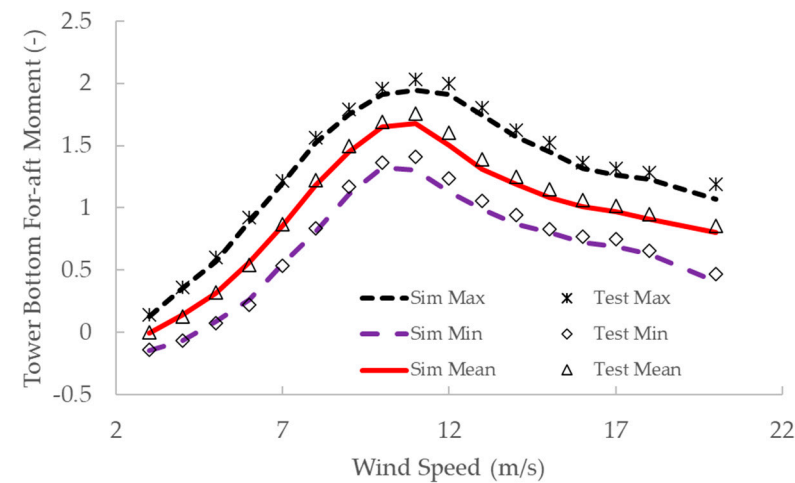**Figure 10.** Comparison of blade root flapwise moments of each wind speed bin.

Figure 11. Comparison of tower bottom fore–aft moments of each wind speed bin.

The blade root flapwise moments of each wind speed bin are compared in Figure 10. The mean values and the maximum and minimum values of the simulation results are, overall, lower than the test results. The largest difference is around −10%, which is still in the reasonable range of engineering practice. The possible reasons for this difference include the inaccuracy of the specified wind shear and turbulence intensity in the rotor

plane, since there were only three measurement points at the met mast in the vertical direction, making the measurement of the wind shear and turbulence intensity incomplete. One may need to look to multipoint laser radar as an advanced method to measure the wind resource.

The tower bottom fore–aft moments of each wind speed bin are examined in Figure 11. The simulation results are again lower than the test results as a consequence of the deviation in the blade root flapwise moments in Figure 10, since the mechanical loads are transmitted from the blades to the tower. However, the difference between the tower bottom fore–aft moments is less than 5%.

Through the code-to-measurement comparisons with the prototype wind turbine, it is evident that the simulation results of the proposed method match the test data reasonably well, and thus the mathematical model is validated.

3.3. Blade Fracture Dynamics Simulation and Validation

As the highlight of this study, a dynamics simulation was performed to reproduce the blade fracture process. The simulation results were compared against the measurement as the final validation.

The aforementioned wind turbine, featuring a rotor diameter of 155 m, was produced and deployed on a large scale. An actual fracture incident occurred on one of the mass wind turbines. Subsequent field investigations identified that one blade was fractured at the spanwise position of approximately 15 m from the blade root.

The online SCADA system of the fractured wind turbine recorded the wind speed and wind direction on the nacelle. In this simulation, the wind speed was set as 9 m/s according to the SCADA data. The wind shear was 0.2. At the moment of the blade fracture, the azimuth angle of the affected blade was 300° (clockwise from the upward direction as 0°). The fractured region spanned from 14 to 16 m from the blade root. The tensile stiffness of the fractured blade section was retained, while bending and torsional stiffness were both set to 0. This corresponds to a fracture mode where the fibers remain intact but the blade is fully split, resulting in an instantaneous fracture. The simulation time for the fracture was set to 60 s. Due to challenges in obtaining precise field data about the fracture location and stiffness variations, there may be some discrepancies in the simulation settings.

In this actual wind turbine blade fracture incident, the time series of the nacelle acceleration were recorded in the SCADA system, but there were no channels for mechanical loads. Consequently, only nacelle accelerations were compared in this study. Figures 12 and 13 present the time-domain signal comparisons of nacelle accelerations in the fore–aft and side–side directions, respectively. The simulation acceleration results exhibit a consistent trend with the field measurement data with comparable magnitudes. The first period of the acceleration fluctuation represents the most dangerous period in the fracture process. The simulation results exhibit a higher amplitude than the measurement data, implying that the simulation is conservative. As time progresses, deviations become more noticeable. It can be noticed that the field measurement data contain more high-frequency components, which are to be attributed to the higher-order modes of the turbine. Nevertheless, the consistency in the trends and magnitudes of the acceleration changes before and after the fracture instant shows that the proposed simulation method is able to replicate blade fracture faults with a moderately conservative result.

Figure 14 illustrates the simulated relative deformation of the blade tip before and after the fracture instant. The out-of-plane and radial relative displacements reach 60 m and 40 m, respectively, which are significantly larger than the results in the normal operation cases. The large displacements of the blade tip are not introduced by the elastic deformation but caused by the large rotation at the blade's fractured section because of the zero bending stiffness settings. It is proved that the proposed geometrically exact beam model is able to tackle the large rotation and large deformation effectively.
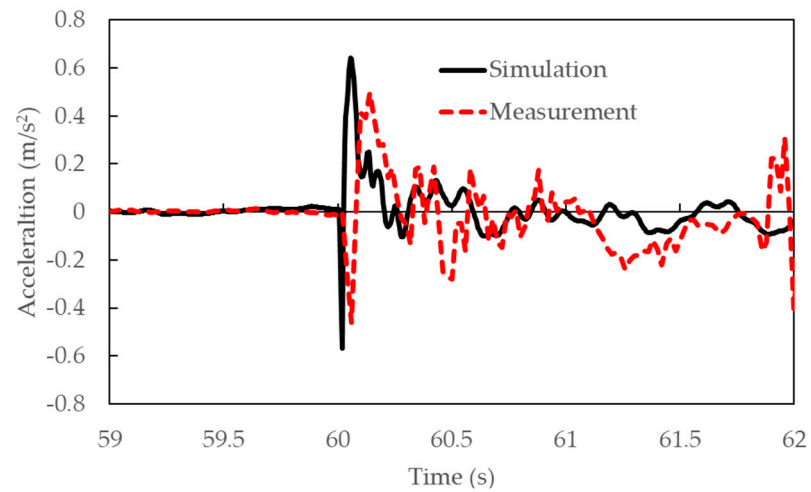
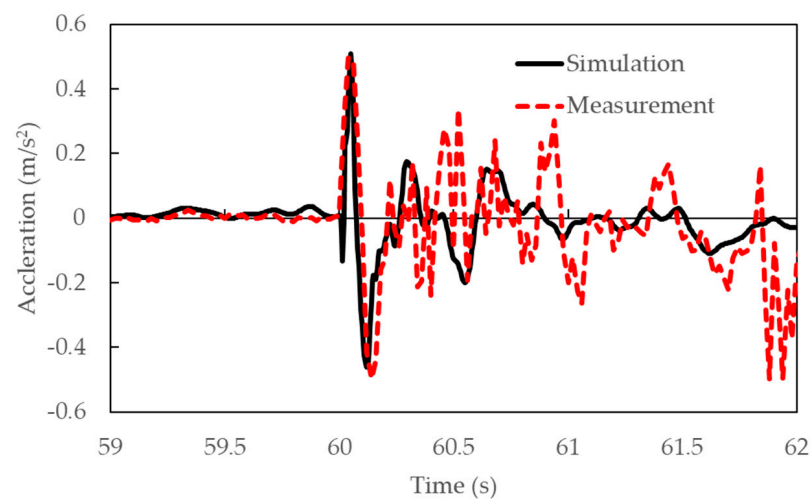**Figure 12.** Comparison of nacelle fore–aft acceleration during fracture.

Figure 13. Comparison of nacelle side–side acceleration during fracture.
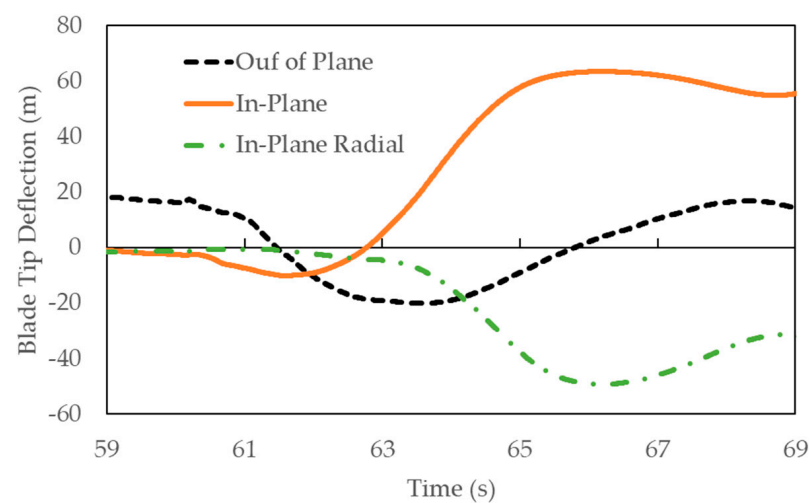

Figure 14. Blade tip deflection during fracture.

4. Conclusions

This paper introduces a simulation method for fracture faults in long and flexible wind turbine blades. Utilizing geometrically exact beam theory, it formulates a nonlinear structural dynamics model for these blades. Additionally, an integrated aeroelastic simulation model is developed by incorporating blade element momentum theory. The accuracy of this aeroelastic simulation model is verified and validated through comparisons with Bladed simulation data and field measurement data on blade fractures. The key research findings are summarized as follows:

1. The geometrically exact beam model for blade structure developed in this study achieves precise nonlinear aeroelastic simulations for entire wind turbines. Under normal operating conditions, the results from this method align with those obtained by Bladed, which employs the multipart modal superposition method.
2. The proposed model is able to effectively simulate the blade fracture process and exhibits trends and magnitudes similar to field measurement data.
3. The simulation results of the blade fracture process provide the load and deformation data, which are difficult to acquire from field measurements. This information is of crucial importance for the root cause analysis of blade fracture faults and for developing and validating monitoring strategies.

The process of blade fracture in wind turbine systems is intricate. While the model presented in this paper successfully reconstructs the most critical aspects of this process, it currently does not account for the blade–tower collision process and the associated changes in structural characteristics. As a result, there is a reduction in the accuracy of this simulation method. Future studies should focus on integrating analyses of the blade failure process, changes in structural characteristics during blade–tower collision, and the establishment of blade sectional stiffness variations. These enhancements will further improve the accuracy of simulating the blade fracture process.

Author Contributions: Methodology, X.W.; Software, X.W.; Writing—original draft, X.W.; Supervision, K.F. and Q.L.; Project administration, X.W. All authors have read and agreed to the published version of the manuscript.

Data Availability Statement: Data are contained within the article.

Conflicts of Interest: The authors declare no conflict of interest.

References

1. Xu, J.; Zhang, L.; Li, X.; Li, S.; Yang, K.J.R.E. A study of dynamic response of a wind turbine blade based on the multi-body dynamics method. *Renew. Energy* **2020**, *155*, 358–368. [CrossRef]
2. Carroll, J.; McDonald, A.; McMillan, D. Failure rate, repair time and unscheduled O&M cost analysis of offshore wind turbines. *Wind Energy* **2016**, *19*, 1107–1119. [CrossRef]
3. Chen, X. Fracture of wind turbine blades in operation—Part I: A comprehensive forensic investigation. *Wind Energy* **2018**, *21*, 1046–1063. [CrossRef]
4. Eder, M.A.; Bitsche, R.D.; Nielsen, M.; Branner, K. A practical approach to fracture analysis at the trailing edge of wind turbine rotor blades. *Wind Energy* **2014**, *17*, 483–497. [CrossRef]
5. Chen, K.; Liu, J.; Guo, W.; Wang, X. A two-stage approach based on Bayesian deep learning for predicting remaining useful life of rolling element bearings. *Comput. Electr. Eng.* **2023**, *109*, 108745. [CrossRef]
6. McGugan, M.; Mishnaevsky, L. Damage Mechanism Based Approach to the Structural Health Monitoring of Wind Turbine Blades. *Coatings* **2020**, *10*, 1223. [CrossRef]
7. Ji, Y.M.; Han, K.S. Fracture mechanics approach for failure of adhesive joints in wind turbine blades. *Renew. Energy* **2014**, *65*, 23–28. [CrossRef]
8. Boyano, A.; Lopez-Guede, J.M.; Torre-Tojal, L.; Fernandez-Gamiz, U.; Zulueta, E.; Mujika, F. Delamination Fracture Behavior of Unidirectional Carbon Reinforced Composites Applied to Wind Turbine Blades. *Materials* **2021**, *14*, 593. [CrossRef]
9. Rosemeier, M.; Berring, P.; Branner, K. Non-linear ultimate strength and stability limit state analysis of a wind turbine blade. *Wind Energy* **2016**, *19*, 825–846. [CrossRef]

10. Wu, G.; Qin, Z.; Zhang, L.; Yang, K. Strain response analysis of adhesively bonded extended composite wind turbine blade suffering unsteady aerodynamic loads. *Eng. Fail. Anal.* **2018**, *85*, 36–49. [CrossRef]
11. Chen, X. Experimental investigation on structural collapse of a large composite wind turbine blade under combined bending and torsion. *Compos. Struct.* **2017**, *160*, 435–445. [CrossRef]
12. Chen, X.; Tang, J.; Yang, K. Modeling multiple failures of composite box beams used in wind turbine blades. *Compos. Struct.* **2019**, *217*, 130–142. [CrossRef]
13. Epaarachchi, J.A.; Clausen, P.D. The development of a fatigue loading spectrum for small wind turbine blades. *J. Wind Eng. Ind. Aerodyn.* **2006**, *94*, 207–223. [CrossRef]
14. Boujleben, A.; Ibrahimbegovic, A.; Lefrançois, E. An efficient computational model for fluid-structure interaction in application to large overall motion of wind turbine with flexible blades. *Appl. Math. Model.* **2020**, *77*, 392–407. [CrossRef]
15. Zhang, C.; Chen, H.-P.; Huang, T.-L. Fatigue damage assessment of wind turbine composite blades using corrected blade element momentum theory. *Measurement* **2018**, *129*, 102–111. [CrossRef]
16. Liu, L.; Bian, H.; Du, Z.; Xiao, C.; Guo, Y.; Jin, W. Reliability analysis of blade of the offshore wind turbine supported by the floating foundation. *Compos. Struct.* **2019**, *211*, 287–300. [CrossRef]
17. Ghasemi, A.R.; Jahanshir, A.; Tarighat, M.H.J.W.; Journal, S.A.I. Numerical and analytical study of aeroelastic characteristics of wind turbine composite blades. *Wind Struct.* **2014**, *18*, 103–116. [CrossRef]
18. Silveira, L.G.C.; Hansen, M.H. Modal Veering Effect on Quadratic Manifold Model Order Reduction Accuracy. Available online: https://ssrn.com/abstract=4466897 (accessed on 2 June 2023).
19. Jensen, C.S.L.; Pedersen, R.B.; Blanco, B.; Escalona, J.L.; Balling, O. On the Combination of Geometrically Nonlinear Models and Substructuring for Multibody Simulation of Wind Turbine Blades. In Proceedings of the ASME 2022 International Design Engineering Technical Conferences and Computers and Information in Engineering Conference, St. Louis, MO, USA, 14–17 August 2022.
20. Kallesøe, B.S. Equations of motion for a rotor blade, including gravity, pitch action and rotor speed variations. *Wind Energy* **2007**, *10*, 209–230. [CrossRef]
21. Yakoub, R.Y.; Shabana, A.A. Three Dimensional Absolute Nodal Coordinate Formulation for Beam Elements: Implementation and Applications. *J. Mech. Des.* **2001**, *123*, 614–621. [CrossRef]
22. Reissner, E. On one dimensional large displacement finite strain beam theory. *Stud. Appl. Math.* **1973**, *52*, 87–95. [CrossRef]
23. Bauchau, O.; Craig, J. Euler-Bernoulli beam theory. In *Structural Analysis: With Applications to Aerospace Structures*; Springer: Berlin/Heidelberg, Germany, 2009; pp. 173–221.
24. Liang, F.Y.; Jiang, Z.; Yuan, Q.; Li, L.; Wang, R. Time-dependent longitudinal responses of a shield tunnel induced by surcharge load: Theoretical prediction and analysis. *Undergr. Space* **2024**, *14*, 219–238. [CrossRef]
25. Lee, H.-K.; Viswamurthy, S.R.; Park, S.C.; Kim, T.; Shin, S.J.; Kim, D.-K. Helicopter Rotor Load Prediction Using a Geometrically Exact Beam with Multicomponent Model. *J. Aircr.* **2010**, *47*, 1382–1390. [CrossRef]
26. Panteli, A.N.; Manolas, D.I.; Riziotis, V.A.; Spiliopoulos, K.V. Comparative study of two geometrically non-linear beam approaches for the coupled wind turbine system. *J. Wind Eng. Ind. Aerodyn.* **2022**, *231*, 105231. [CrossRef]
27. Wang, L.; Liu, X.; Renevier, N.; Stables, M.; Hall, G.M. Nonlinear aeroelastic modelling for wind turbine blades based on blade element momentum theory and geometrically exact beam theory. *Energy* **2014**, *76*, 487–501. [CrossRef]
28. Chen, J.G.; Shen, X.; Wang, G.; Sun, C.; Zhu, X.C.; Du, Z.H. Aeroelastic modeling for wind turbine blade based on lifting surface model and nonlinear beam theory. *K. Cheng Je Wu Li Hsueh Pao/J. Eng. Thermophys.* **2018**, *39*, 1469–1475.
29. Fleming, I.; Luscher, D. A model for the structural dynamic response of the CX-100 wind turbine blade. *Wind Energy* **2014**, *17*, 877–900. [CrossRef]
30. Overgaard, L.C.T.; Lund, E. Damage Analysis of a Wind Turbine Blade. In Proceedings of the ECCOMAS Thematic Conference on Mechanical Response of Composites, Porto, Portugal, 22–24 September 2007.
31. Bauchau, O.A.; Han, S.; Mikkola, A.; Matikainen, M.K. Comparison of the absolute nodal coordinate and geometrically exact formulations for beams. *Multibody Syst. Dyn.* **2014**, *32*, 67–85. [CrossRef]
32. Otsuka, K.; Makihara, K.; Sugiyama, H. Recent Advances in the Absolute Nodal Coordinate Formulation: Literature Review From 2012 to 2020. *ASME J. Comput. Nonlinear Dyn.* **2022**, *17*, 080803. [CrossRef]
33. Lü, P.; Liao, M.; Xu, Y.; Yin, Y. Beam Finite Element for Wind Turbine Bladebased on Geometrically Exact Beam Theory. *Acta Energiae Solaris Sin.* **2015**, *36*, 2422–2428.
34. Qian, X.; Gao, Z.; Wang, T.; Wang, L.; Ke, S. Nonlinear aeroelastic response analysis of 100-meter-scale flexible wind turbine blades. *Acta Aerodyn. Sin.* **2022**, *40*, 220–230.
35. Pin, L.; Mingfu, L.; Siji, W. Predictions of wind turbine aerodynamics based on lifting surface theory with fully free vortex and the influence of the parameters. *Mach. Des. Manuf.* **2017**, *3*, 52–55.
36. Horcas, S.G.; Madsen, M.H.; Sørensen, N.N.; Zahle, F.; Barlas, T. Influence of the installation of a trailing edge flap on the vortex induced vibrations of a wind turbine blade. *J. Wind Eng. Ind. Aerodyn.* **2022**, *229*, 105118. [CrossRef]
37. Grinderslev, C.; Houtin-Mongrolle, F.; Sørensen, N.N.; Pirrung, G.R.; Jacobs, P.; Ahmed, A.; Duboc, B. Forced-motion simulations of vortex-induced vibrations of wind turbine blades—A study of sensitivities. *Wind Energy Sci.* **2023**, *8*, 1625–1638. [CrossRef]
38. Madsen, H.A.; Larsen, T.J.; Pirrung, G.R.; Li, A.; Zahle, F. Implementation of the blade element momentum model on a polar grid and its aeroelastic load impact. *Wind Energy Sci.* **2020**, *5*, 1–27. [CrossRef]

39. Han, S.; Bauchau, O.A. On the global interpolation of motion. *Comput. Methods Appl. Mech. Eng.* **2018**, *337*, 352–386. [CrossRef]
40. Guodong, R.; Wenlei, S.; Xiuling, R. Fatigue research on vane of wind power generator based on cosimulation. *Mach. Tool Hydraul.* **2010**, *38*, 100–102.
41. Douvi, E.; Douvi, D. Aerodynamic Characteristics of Wind Turbines Operating under Hazard Environmental Conditions: A Review. *Energies* **2023**, *16*, 7681. [CrossRef]
42. DNV-GL Garrad Hassan. Bladed Software. Available online: https://www.dnv.com/services/wind-turbine-design-software-bladed-3775 (accessed on 28 January 2024).
43. *IEC 61400-13*; Wind Turbine Generator Systems—Part 13: Measurement of Mechanical Loads. Technical Report, First Edition. International Electrotechnical Commission: Geneva, Switzerland, 2001.